Journal of Catalysis 256 (2008) 248–258

Contents lists available at ScienceDirect

Journal of Catalysis

www.elsevier.com/locate/jcat

Mechanistic origin of the different activity of Rh-ZSM-5 and Fe-ZSM-5 in N_2O decomposition

Evgenii V. Kondratenko [a,*], Vita A. Kondratenko [a], Marta Santiago [b], Javier Pérez-Ramírez [b,c,*]

[a] Leibniz-Institut für Katalyse e. V. an der Universität Rostock, Außenstelle Berlin, Richard-Willstätter-Str. 12, D-12489, Berlin, Germany
[b] Institute of Chemical Research of Catalonia (ICIQ), Avinguda Països Catalans 16, 43007, Tarragona, Spain
[c] Catalan Institution for Research and Advanced Studies (ICREA), Passeig Lluís Companys 23, 08010, Barcelona, Spain

ARTICLE INFO

Article history:
Received 23 October 2007
Revised 17 March 2008
Accepted 21 March 2008
Available online 1 May 2008

Keywords:
N_2O decomposition
Metal zeolites
Rh-ZSM-5
Fe-ZSM-5
Oxygen formation
Mechanism
Kinetics
TAP reactor

ABSTRACT

A temporal analysis of products (TAP) reactor was used to study relationships between the mechanism of direct N_2O decomposition over metal-loaded zeolites and their resulting activity. Rh-ZSM-5 (prepared by incipient wetness) and Fe-ZSM-5 (prepared by liquid-ion exchange) were chosen as prototypic catalysts displaying low (<550 K) and high (>650 K) temperature activity, respectively. Transient studies at the same contact time revealed the higher activity of Rh-ZSM-5 below 623 K and significantly stronger N_2O adsorption over Rh species than over Fe species in the zeolites. Several microkinetic models were applied for simultaneous fitting the transient responses of N_2O, N_2, and O_2. Classical reaction schemes failed to describe the experimental data. The preferred models of N_2O decomposition over Rh-ZSM-5 and Fe-ZSM-5 differ in the reaction pathways of O_2 formation. For both catalysts, free active metal sites (*) and those occupied by monoatomic oxygen species (*-O) from N_2O participate in the decomposition of gas-phase N_2O. Gas-phase O_2 is formed directly on N_2O interaction with *-O over Rh-ZSM-5, whereas the latter reaction over Fe-ZSM-5 leads to a surface bi-atomic oxygen species (O-*-O), followed by its transformation to *-O_2. The latter species desorbs as molecular oxygen. Comparison of ion-exchanged and steam-activated Fe-ZSM-5 [J. Phys. Chem. B 110 (2006) 22586] revealed that the reaction mechanism is independent of the iron constitution induced by the preparation and activation routes, despite important differences in catalytic activity. Our quantitative microkinetic analysis demonstrated that both the stronger reversible N_2O adsorption and, most importantly, the faster desorption of O_2 are distinctive mechanistic features of Rh-ZSM-5, likely indicating its high de-N_2O activity.

1. Introduction

Metal-loaded zeolites are efficient catalysts for direct N_2O decomposition into N_2 and O_2. A number of metals (i.e., Fe, Co, Ni, Cu, Mn, Ce, Ru, Rh, Pd, Pt) deposited in various zeolite structures (especially ZSM-5, but also ZSM-11, beta, mordenite, USY, ferrierite, zeolites A, and X) has been reported as active components for this reaction [1]. It is generally accepted that the catalytic activity is determined by the combination of the metal ion, the zeolite matrix, and the preparation method. For the Me-ZSM-5 system, Li and Armor [2] determined the following activity order of metals: Rh ~ Ru > Pd > Cu > Co > Fe > Pt > Ni > Mn. Rh-ZSM-5 is active for N_2O decomposition below 550 K. The low-temperature activity of the rhodium system is not exclusive of the zeolite, because Rh on other supports, such as Al_2O_3 [3,4], TiO_2 [5], ZrO_2 [6,7], ZnO [8], CeO_2 [9], and calcined hydrotalcites [10–13], is active even at 450 K. Despite the remarkably low-temperature activity of rhodium-catalysts, iron-containing zeolites (especially Fe-ZSM-5) have attracted more attention from academy and industry [14]. In contrast to Rh-ZSM-5, Fe-ZSM-5 exhibits activity at higher temperature (typically above 650 K). The activity of Fe-ZSM-5 can be increased by steam activation [15] and high-temperature treatment in inert atmosphere or vacuum [16,17]. To date, however, no synthesis route or activation protocol has generated Fe-ZSM-5 catalysts that approach the activity of Rh-based materials in terms of N_2O conversion using the same contact time. Nonetheless, the remarkable de-N_2O performance of Fe-ZSM-5 in the presence of additional gases, such as O_2, NO, and H_2O, as well as the low cost compared with the noble metal, represent major advantages for industrial implementation (e.g., in the tail-gas train of nitric acid plants) [4].

The aforementioned features of Fe-ZSM-5 have stimulated many studies aimed at elucidating the role of the nature of active iron species in N_2O decomposition [15–26] and deriving reaction kinetics [16,23,25,27–38]. The decomposition of N_2O to N_2 and O_2 has been classically described by models derived from schemes A

* Corresponding authors.
E-mail addresses: evgenii.kondratenko@catalysis.de (E.V. Kondratenko), jperez@iciq.es (J. Pérez-Ramírez).

0021-9517/$ – see front matter
doi:10.1016/j.jcat.2008.03.016

Classical scheme A [27]

$N_2O + * \rightarrow N_2 + *\text{-}O$

$N_2O + *\text{-}O \rightarrow N_2 + O_2 + *$

Classical scheme B [20]

$N_2O + * \rightarrow N_2 + *\text{-}O$

$*\text{-}O + *\text{-}O \rightarrow O_2 + 2*$

DFT-derived scheme [34,35,38]

$N_2O + * \rightarrow N_2 + *\text{-}O$

$N_2O + *\text{-}O \rightarrow N_2 + *\text{-}O_2$

$N_2O + *\text{-}O_2 \rightarrow *\text{-}O_3 + N_2$

$*\text{-}O_3 \rightarrow O_2 + *\text{-}O$

TAP-derived scheme [36,37]

$N_2O + * \rightarrow N_2 + *\text{-}O$

$N_2O + *\text{-}O \rightarrow N_2 + O\text{-}*\text{-}O$

$O\text{-}*\text{-}O \rightarrow *\text{-}O_2$

$*\text{-}O_2 \rightarrow O_2 + *$

Fig. 1. Summary of reported mechanistic schemes of N_2O decomposition.

and B in Fig. 1. These models differ basically in terms of the mechanism of O_2 formation. Recent microkinetic investigations have revealed that the mechanism of N_2O decomposition over Fe-ZSM-5 is more complex than the classical concepts. Models derived from density functional theory (DFT) calculations [34,35,38] and from transient studies in a temporal analysis of products (TAP) reactor over steam-activated Fe-ZSM-5 and Fe-silicalite [36,37] excluded the recombination of two adsorbed oxygen species as a possible pathway leading to O_2, but considered the reaction between gas-phase N_2O and surface oxygen species deposited by N_2O over free iron sites. According to the latest kinetic schemes, gas-phase O_2 is formed via a complex sequence of surface–surface or gas–surface reactions (Fig. 1, bottom). Both DFT- and TAP-derived models were validated by extrapolation over a broad range of reaction conditions.

In contrast to those of iron-containing zeolites, mechanistic investigations of N_2O decomposition over rhodium-based catalysts are scarce. Kunimori and co-workers [39,40] studied the mechanism of O_2 formation over Rh black and Rh-USY using isotopically labeled $^{18}O_2$. Taking into account the distribution of labeled oxygen atoms in O_2 produced on $N_2{}^{16}O$ pulsing over the $^{18}O_2$-pretreated catalyst, it was concluded that gas-phase oxygen originates from recombination of two surface atomic oxygen species ($*\text{-}O + *\text{-}O \rightarrow O_2 + 2*$).

To the best of our knowledge, the mechanism of N_2O decomposition over rhodium- and iron-containing catalysts has not been studied using the same platforms (experimental or theoretical) and the same zeolite matrix (ZSM-5). In particular, elucidating intrinsic mechanistic features responsible for their different de-N_2O activity appears to be of great fundamental importance. For this purpose, we have performed transient experiments in the TAP reactor over ion-exchanged Fe-ZSM-5 and impregnated Rh-ZSM-5 catalysts in the temperature range of 373–873 K. Different microkinetic models were quantitatively evaluated and discriminated by simultaneous fitting of the transient responses of N_2O, N_2, and O_2. The choice of a liquid-ion exchange method for Fe-ZSM-5 also made it possible to compare the mechanism over this sample with our previous microkinetic analyses over steam-activated Fe-ZSM-5 and Fe-silicalite [36]. This comparison is essential to determine whether the distinct N_2O decomposition activity of differently synthesized and activated iron zeolites obeys to a mechanistic difference associated with the iron speciation or postsynthesis catalyst treatment.

2. Experimental

2.1. Catalysts

The commercial ZSM-5 zeolite used in this study was supplied by Zeolyst (CBV 3024E, NH_4 form, nominal molar Si/Al = 15). Before metal incorporation, the zeolite was dried at 353 K for 24 h. Rh-ZSM-5 was prepared by an incipient-wetness method, using $RhCl_3$ as the metal precursor to achieve a nominal loading of 0.5 wt% Rh. The sample was dried at 353 K for 12 h. Instead of the steam-activation method applied to prepare Fe-MFI samples in our previous TAP study [36], in the present study Fe-ZSM-5 was prepared by liquid-ion exchange with $Fe(NO_3)_3{\cdot}9H_2O$ at a nominal loading of 1.0 wt% Fe. The exchange was carried out at room temperature under vigorous stirring for 18 h. The resulting zeolite was filtered, washed thoroughly, and dried at 353 K for 12 h. The dried solids were finally calcined in static air at 873 K for 5 h at a heating rate of 5 K min^{-1}.

The rhodium and iron content in the zeolites was determined by inductively coupled plasma–optical emission spectroscopy (ICP-OES) (Perkin-Elmer Optima 3200RL [radial]). Powder X-ray diffraction (XRD) patterns were acquired using a Bruker AXS D8 Advance diffractometer equipped with a Cu tube, a Ge(111) incident beam monochromator ($\lambda = 0.1541$ nm), and a Vantec-1 PSD. Data were recorded in the 2θ range of 5 to 55° with an angular step size of 0.02° and a counting time of 5 s per step. Transmission electron microscopy (TEM) was carried out using a JEOL JEM-1011 microscope operated at 100 kV. A few droplets of the sample suspended in ethanol were placed on a carbon-coated copper grid, followed by evaporation under ambient conditions. N_2 adsorption–desorption isotherms at 77 K were measured on a Quantachrome Autosorb 1MP analyzer. The micropore volume and the mesopore surface area were determined using the *t*-plot method [41]. The BET method [42] was used to calculate the total surface area of the samples.

2.2. Transient experiments in vacuum

Mechanistic investigations of N_2O decomposition over the catalysts were performed in a TAP-2 reactor, which is a transient pulse technique with sub-millisecond time resolution [43,44]. The catalyst sample (sieve fraction 250–350 μm) was packed within the isothermal zone of the quartz microreactor (40 mm long; 6 mm i.d.) between two layers of quartz particles of the same sieve fraction. Transient experiments for kinetic evaluation were carried out with 25 mg of Fe-ZSM-5 and 10 mg of Rh-ZSM-5. The catalyst was pretreated in flowing O_2 (30 ml STP min^{-1}) at 773 K and atmospheric pressure for 1 h, followed by exposure to vacuum (10^{-5} Pa) and cooling to 373 K. Thereafter, a mixture of N_2O:Ne = 1:1 was pulsed in the temperature range of 373–873 K, starting at 373 K and increasing in intervals of 25–100 K. The ramping from one temperature to the next was done in vacuum. Approximately 30 min after each setpoint was reached, the mixture of N_2O and Ne was pulsed. The degree of N_2O conversion was calculated at each temperature. The pulse size was in the range of 5×10^{14}–1×10^{15} molecules. Under these conditions, Knudsen diffusion describes the transport of the gaseous components inside the reactor and the transient responses are a function of gas–solid interactions; that is, they are not influenced by molecular collisions in the gas phase.

A quadrupole mass spectrometer (HAL RC 301; Hiden Analytical) was used for the quantitative analysis of reactants and reaction products. The transient responses at the reactor outlet were monitored at the following atomic mass units (AMU): 44 for N_2O, 32 for O_2, 30 for N_2O and NO, 28 for N_2 and N_2O, and 20 for Ne. In the experiments, 10 pulses for each AMU were averaged to improve the signal-to-noise ratio. The concentrations of feed components and reaction products were determined from the corresponding AMUs using standard fragmentation patterns and sensitivity factors according to the procedure outlined in Appendix A.

Table 1
Micro-kinetic models evaluated in this work

Model	Elementary reaction step	
1	$N_2O + * \rightarrow N_2 + *\text{-}O$	(1.1)
	$*\text{-}O + *\text{-}O \rightarrow O_2 + 2*$	(1.2)
2	$N_2O + * \rightarrow N_2 + *\text{-}O$	(2.1)
	$N_2O + *\text{-}O \rightarrow N_2 + O_2 + *$	(2.2)
3	$N_2O + * \rightarrow N_2 + *\text{-}O$	(3.1)
	$*\text{-}O + *\text{-}O \rightarrow *\text{-}O_2 + *$	(3.2)
	$*\text{-}O_2 \rightarrow O_2 + *$	(3.3)
4	$N_2O + * \rightarrow N_2 + *\text{-}O$	(4.1)
	$N_2O + *\text{-}O \rightarrow N_2 + *\text{-}O_2$	(4.2)
	$N_2O + *\text{-}O_2 \rightarrow N_2 + O\text{-}*\text{-}O_2$	(4.3)
	$O\text{-}*\text{-}O_2 \rightarrow O_2 + *\text{-}O$	(4.4)
	$*\text{-}O_2 \rightarrow O_2 + *$	(4.5)
5	$N_2O + * \rightarrow *\text{-}O + N_2$	(5.1)
	$N_2O + *\text{-}O \rightarrow O\text{-}*\text{-}O + N_2$	(5.2)
	$O\text{-}*\text{-}O \rightarrow *\text{-}O_2$	(5.3)
	$*\text{-}O_2 \rightarrow O_2 + *$	(5.4)
6	$N_2O + * \rightarrow *\text{-}N_2O$	(6.1)
	$*\text{-}N_2O \rightarrow N_2O + *$	(6.2)
	$*\text{-}N_2O \rightarrow N_2 + *\text{-}O$	(6.3)
	$*\text{-}O + *\text{-}O \rightarrow O_2 + 2*$	(6.4)
7	$N_2O + * \rightarrow *\text{-}N_2O$	(7.1)
	$*\text{-}N_2O \rightarrow N_2O + *$	(7.2)
	$*\text{-}N_2O \rightarrow N_2 + *\text{-}O$	(7.3)
	$*\text{-}O + *\text{-}O \rightarrow *\text{-}O_2 + *$	(7.4)
	$*\text{-}O_2 \rightarrow O_2 + *$	(7.5)
8	$N_2O + * \rightarrow *\text{-}N_2O$	(8.1)
	$*\text{-}N_2O \rightarrow N_2O + *$	(8.2)
	$*\text{-}N_2O \rightarrow N_2 + *\text{-}O$	(8.3)
	$N_2O + *\text{-}O \rightarrow O_2 + * + N_2$	(8.4)
9	$N_2O + * \rightarrow *\text{-}N_2O$	(9.1)
	$*\text{-}N_2O \rightarrow N_2O + *$	(9.2)
	$*\text{-}N_2O \rightarrow N_2 + *\text{-}O$	(9.3)
	$N_2O + *\text{-}O \rightarrow *\text{-}O_2 + N_2$	(9.4)
	$*\text{-}O_2 \rightarrow * + O_2$	(9.5)
10	$N_2O + * \rightarrow *\text{-}N_2O$	(10.1)
	$*\text{-}N_2O \rightarrow N_2O + *$	(10.2)
	$*\text{-}N_2O \rightarrow N_2 + *\text{-}O$	(10.3)
	$N_2O + *\text{-}O \rightarrow O_2 + N_2 + *$	(10.4)
	$*\text{-}O + *\text{-}O \rightarrow O_2 + 2*$	(10.5)
11	$N_2O + * \rightarrow *\text{-}N_2O$	(11.1)
	$*\text{-}N_2O \rightarrow N_2O + *$	(11.2)
	$*\text{-}N_2O \rightarrow N_2 + *\text{-}O$	(11.3)
	$N_2O + *\text{-}O \rightarrow * + O_2 + N_2$	(11.4)
	$O_2 + * \rightarrow *\text{-}O_2$	(11.5)
	$*\text{-}O_2 \rightarrow O_2 + *$	(11.6)
	$*\text{-}O_2 + * \rightarrow 2*\text{-}O$	(11.7)
	$2*\text{-}O \rightarrow *\text{-}O_2 + *$	(11.8)

2.3. Kinetic evaluation of transient experiments

The parameter estimation procedure used here has been described in detail previously [45,46]. In brief, it is based on a numerical solution of partial differential equations (PDEs) describing processes of diffusion, adsorption, desorption, and reaction in the TAP microreactor. PDEs are transformed into coupled ordinary differential equations (ODEs) by spatial approximation and then integrated numerically using the PDEONE routine [47]. Parameters (i.e., rate and diffusion coefficients) were determined using first a genetic algorithm to find good starting values [48] and then the Nelder-Mead simplex algorithm [49]. The TAP microreactor was described as a one-dimensional pseudohomogeneous system divided into three zones, represented by the catalyst and the two layers of inert material, in which the zeolite is sandwiched. The goodness of fit was determined by an objective function defined as the sum of squares of the shortest deviations between the respective pairs of points of the experimental and simulated transients [46].

Table 2
Characterization data of the samples investigated in this study

Sample	Metal content in solid (wt%)	V_{pore} ($cm^3\,g^{-1}$)	V_{micro} ($cm^3\,g^{-1}$)	S_{BET} ($m^2\,g^{-1}$)
H-ZSM-5	–	0.32	0.17	410
Fe-ZSM-5	0.8 (1.0)[a]	0.34	0.16	417
Rh-ZSM-5	0.4 (0.5)	0.28	0.13	320

[a] Nominal metal loadings between brackets.

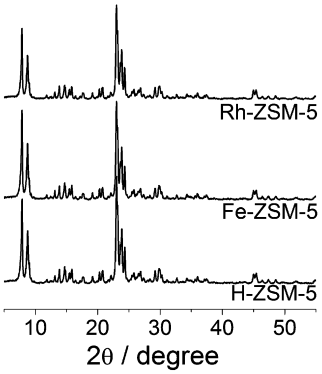

Fig. 2. X-ray diffraction patterns of the zeolites.

The microkinetic models of direct N_2O decomposition evaluated in this work are listed in Table 1. Intracrystalline diffusion was neglected in the models, because Keipert and Baerns [50] have shown that this process had a minor influence on the shape of transient responses of inert gases on pulsing in the TAP microreactor. The transport of gaseous compounds was described by Knudsen diffusion along the reactor axis. Additional details on the procedure for kinetic evaluation of transient experiments are provided in Appendix B. Based on the results of the model discrimination at the reference temperature (T_{ref}), the best model was selected for fitting the transient responses at other temperatures. To avoid the correlation between activation energies and pre-exponential factors [51,52], activation energies for all elementary reaction steps were derived according to the equation

$$k_{T_i} = k_{T_{ref}} \cdot \exp\left(-\frac{E_a}{R} \cdot \left(\frac{1}{T_i} - \frac{1}{T_{ref}}\right)\right),$$

where T_{ref} and $k_{T_{ref}}$ are the reference temperature and rate coefficient at this temperature, respectively. Following [51], the reference temperature was centered within the temperature range applied in the experiments.

3. Results and discussion

3.1. Catalysts

Table 2 shows the results of the catalyst characterization. The iron and rhodium contents in the samples were close to the nominal metal loading. The XRD pattern of the parent H-ZSM-5 zeolite was not altered on incorporation of the metal, and no additional reflections belonging to new crystalline phases were identified (Fig. 2). TEM indicated the presence of metal oxide nanoparticles in the samples with a rather uniform size distribution (Fig. 3). The oxide particles ranged in size from 4 to 6 nm in Fe-ZSM-5, compared with 2–5 nm in Rh-ZSM-5. As could be expected due to the different synthesis methods applied, the iron speciation in the ion-exchanged Fe-ZSM-5 differed from that in the steam-activated Fe-ZSM-5 and Fe-silicalite used in our previous kinetic study of N_2O decomposition [36]. The degree of iron clustering in the former sample was significantly more pronounced, as is typical in iron zeolites prepared by liquid-ion exchange [22]. This results in

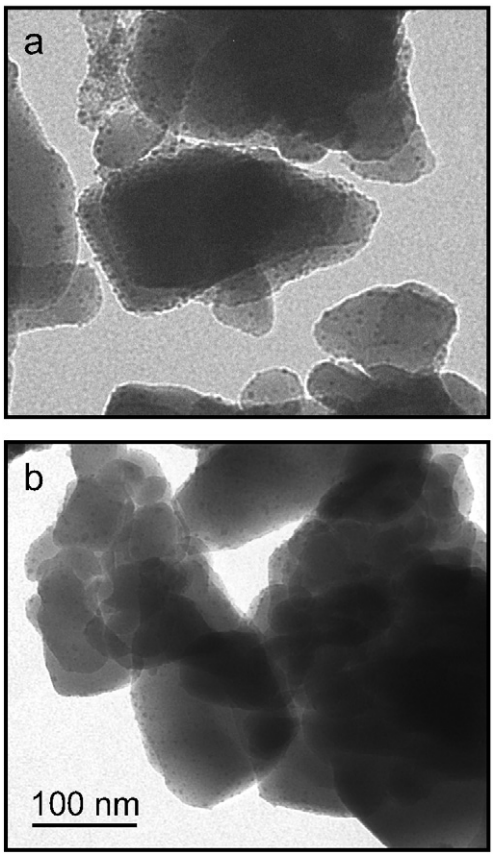

Fig. 3. TEM micrographs of (a) Fe-ZSM-5 and (b) Rh-ZSM-5.

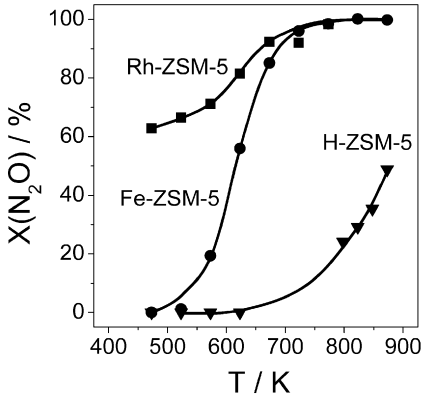

Fig. 4. N_2O conversion versus temperature over the zeolites under transient conditions (N_2O:Ne = 1:1, pulse size ca. 10^{15}, catalyst amount = 50 mg).

lower N_2O decomposition activity [53]. The porous properties of the H-ZSM-5 and Fe-ZSM-5 samples were very similar, whereas Rh-ZSM-5 showed a slightly decreased micropore volume and specific surface area, likely related to the blockage of micropores by rhodium oxide particles.

3.2. Transient activity in N_2O decomposition

To investigate whether the activity order of H-ZSM-5, Fe-ZSM-5, and Rh-ZSM-5 in N_2O decomposition under ambient pressure steady-state conditions (Rh > Fe > H) [1,2] also is valid for the transient vacuum conditions in the TAP reactor, single N_2O pulse experiments were performed in the temperature range of 473–873 K. The sample amount was fixed to 50 mg, to allow a good comparison of the activity of the various catalysts. Fig. 4 shows

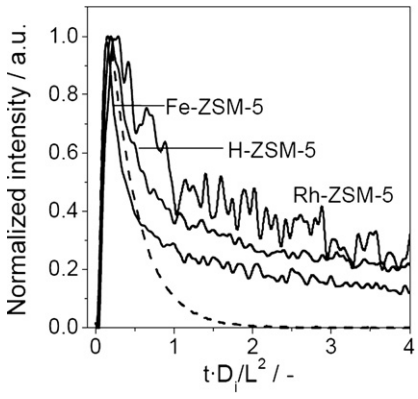

Fig. 5. Normalized transient responses of N_2O and Ne (dashed line) upon N_2O pulsing over H-ZSM-5, Rh-ZSM-5, and Fe-ZSM-5 at 373 K (N_2O:Ne = 1:1, pulse size ca. 10^{15}, catalyst amount = 50 mg).

the conversion of N_2O versus temperature. Rh-ZSM-5 exhibited the highest activity, particularly below 600 K; for example, the N_2O conversion over Rh-ZSM-5 at 500 K was ca. 65%, whereas Fe-ZSM-5 was inactive at this temperature. As expected, the lowest activity was observed over H-ZSM-5, which required temperatures above 650 K to exhibit some N_2O conversion. This indicates that the order of catalyst activity in N_2O decomposition is not influenced by the operation mode (i.e., vacuum and transient vs high pressure and steady-state). Based on this finding, we focus on the analysis and kinetic evaluation of transient experiments performed in the TAP reactor.

3.3. Mechanistic studies

Based on the simulation-free mechanistic analysis of the TAP data [43], here we use the results of N_2O transient experiments in the temperature range 373–823 K to elucidate the N_2O-adsorptive properties of the catalysts and the possible role of NO in N_2O decomposition. In turn, in Section 3.4 we use this information to build microkinetic models of N_2O decomposition, which we apply for kinetic evaluation of N_2O pulse experiments over Rh-ZSM-5 and Fe-ZSM-5.

To evaluate whether N_2O is reversibly adsorbed over H-ZSM-5, Fe-ZSM-5, and Rh-ZSM-5, we analyzed the shape of the transient responses of N_2O, and Ne at low temperatures, which facilitates investigation of the adsorption process. Following [43], we transformed the time scale of the transient responses of N_2O and Ne on pulsing an N_2O:Ne = 1:1 mixture into dimensionless form. The dimensionless time is defined as $t \cdot D_i/L^2$, where t is the pulse time, D_i is the effective diffusion coefficient of each component, and L is the reactor length. This normalization makes it possible to exclude the effect of the diffusion transport on the shape of the transient responses of different components. Moreover, important mechanistic insights into reversible/irreversible adsorption of N_2O can be directly extracted from the normalized experimental data with no further mathematical treatment.

The normalized transients of N_2O and Ne recorded at 373 K are presented in Fig. 5. No visible differences in the normalized Ne responses over H-ZSM-5, Fe-ZSM-5, and Rh-ZSM-5 were identified, indicating that the transport processes were very similar for all catalysts. Therefore, the different shapes of the normalized N_2O responses shown in Fig. 5. for the various catalysts are due to the differences in the catalyst's N_2O-adsorptive properties. It is important to stress that we used the same zeolite matrix for the preparation of all catalysts. This allows us to discriminate between the N_2O-adsorptive properties of zeolite itself and those of the active metals (Rh and Fe). Among the catalysts, the N_2O response over Rh-ZSM-5 was the broadest and had the longest

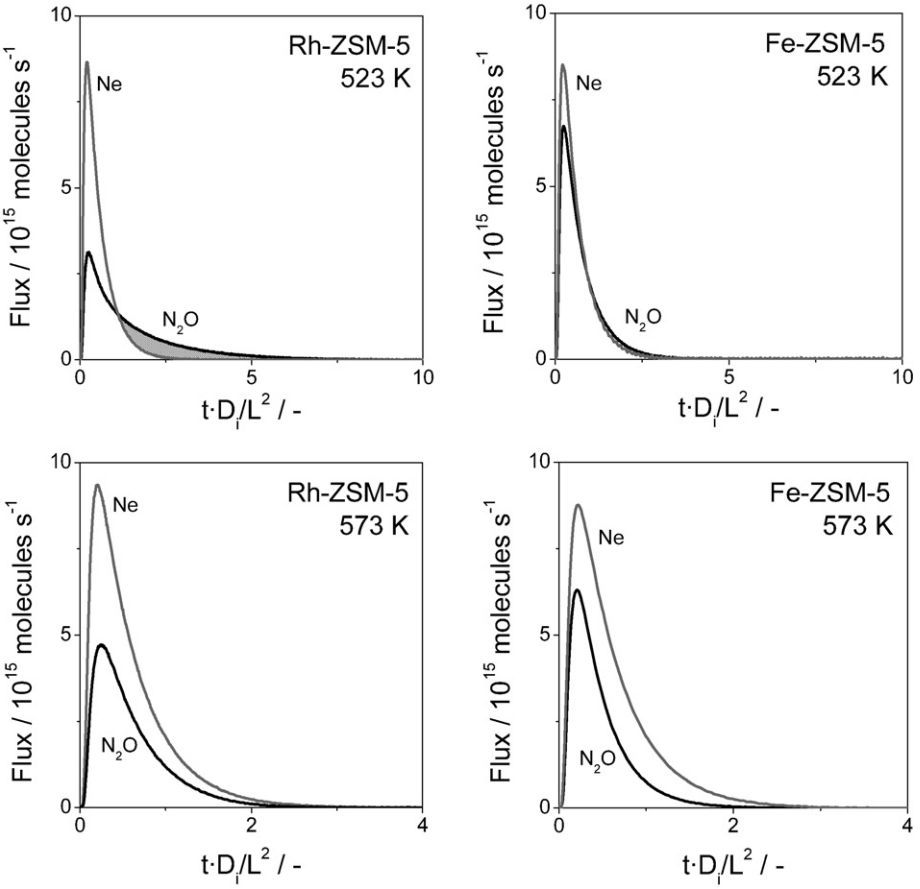

Fig. 6. Normalized transient responses of N_2O and Ne upon N_2O pulsing over Rh-ZSM-5 (10 mg) and Fe-ZSM-5 (25 mg) at 523 and 573 K (N_2O:Ne = 1:1, pulse size ca. 10^{15}).

tailing, whereas that over Fe-ZSM-5 was the sharpest and had the shortest tailing. According to the TAP theory [43], this indicates that N_2O adsorbed strongly over all of the catalysts. With respect to N_2O desorption, the catalysts can be ordered as follows: Fe-ZSM-5 > H-ZSM-5 > Rh-ZSM-5. The slightly higher desorption of N_2O from Fe-ZSM-5 compared with H-ZSM-5 may be due to the blockage of strong adsorption sites in the bare zeolite by FeO_x species. Based on their transient experiments, Kiwi-Minsker et al. [16,24] concluded that ZSM-5 with low iron content (up to 1000 ppm) reversibly adsorbs N_2O; however, they provided no experimental evidence demonstrating whether N_2O adsorbs over iron species and/or over the zeolite support. As our results in Fig. 5. demonstrate, we cannot unambiguously conclude that the additional iron in the ion-exchanged Fe-ZSM-5 enhances the adsorption properties of H-ZSM-5; however, the differences in the normalized N_2O responses over H-ZSM-5 (Fe-ZSM-5) and Rh-ZSM-5 do suggest that N_2O adsorption over Rh-ZSM-5 occurs over active metal sites.

Because the adsorption/desorption properties of the materials are influenced by temperature, we analyzed the normalized N_2O and Ne responses over Fe-ZSM-5 and Rh-ZSM-5 at 523 and 573 K. Generally, N_2O desorption should increase more strongly with temperature than N_2O adsorption. The normalized N_2O and Ne transients are presented in Fig. 6. The degree of N_2O conversion at 523 K was ca. 30% over Rh-ZSM-5 and <5% over Fe-ZSM-5. Despite the high N_2O conversion over Rh-ZSM-5, the normalized N_2O transient response was not simply situated inside the normalized transient of Ne, as the TAP theory predicts for the case of irreversible reaction (i.e., N_2O decomposition) [43]; instead, it crossed the normalized Ne transient response (diffusion only). Such an intersection is the "fingerprint" for reversible N_2O adsorption. Taking into account the long tailing of the N_2O transients, we can conclude that N_2O strongly adsorbed and slowly desorbed over Rh-ZSM-5. In contrast, no long tailing of the N_2O response was observed over Fe-ZSM-5 (Fig. 6), indicating no significant N_2O adsorption. Alternatively, the rates of adsorption and desorption over Fe-ZSM-5 were comparable (i.e., weak N_2O adsorption).

The degree of N_2O conversion was 15% over Fe-ZSM-5 and 50% over Rh-ZSM-5 at 573 K. Fig. 6 clearly shows that the normalized transient response of N_2O over Fe-ZSM-5 was considerably sharper and located inside the normalized transient response of Ne compared with that obtained at 523 K. Based on [43], we can conclude that N_2O was irreversibly decomposed over this catalyst. It is important to note that the normalized transient of N_2O over Rh-ZSM-5 also was located inside the Ne transient response but was significantly broader than that over Fe-ZSM-5, despite a considerably higher degree of N_2O conversion. This result further supports the stronger reversible N_2O adsorption over Rh-ZSM-5 than over Fe-ZSM-5. Thus, the rhodium- and iron-containing catalysts have different properties for adsorption and desorption of N_2O in the same temperature range.

Further mechanistic insights into N_2O decomposition also were derived from the height-normalized transient responses of N_2O and the decomposition products at different temperatures. Fig. 7 compares the transients of N_2, O_2, and signals detected at AMUs of 44 and 30. The signal at AMU of 44 belongs to N_2O (CO_2 can be excluded, because the catalysts were pretreated in an O_2 flow for 1 h at 773 K), whereas the signal at AMU of 30 can be associated with N_2O and/or NO. Nitric oxide was previously considered to be an intermediate in N_2O decomposition over Fe-ZSM-5 catalysts [32, 54]. If NO was formed in these experiments, then the shape of the signal at AMU of 30 should differ from that at AMU of 44; however, as shown in Fig. 7 the height-normalized transients at AMUs

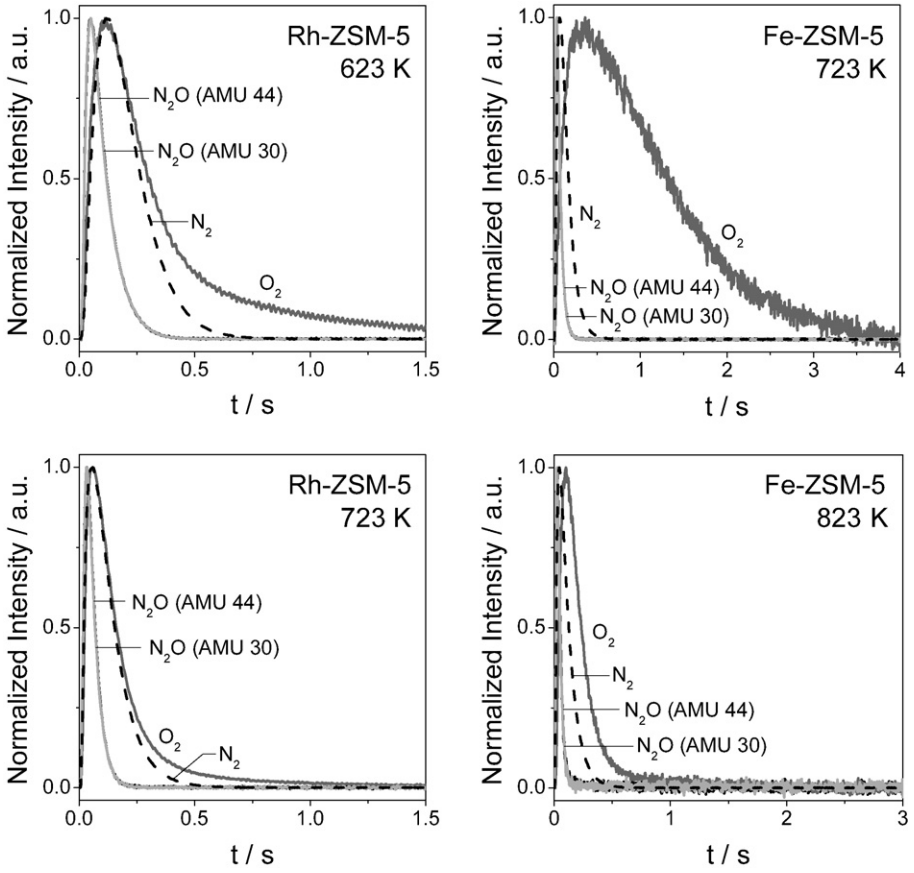

Fig. 7. Height-normalized transient responses of N_2O, N_2, and O_2 upon N_2O pulsing over Rh-ZSM-5 (10 mg), and Fe-ZSM-5 (25 mg) at different temperatures (N_2O:Ne = 1:1, pulse size ca. 10^{15}).

of 44 and 30 had very similar shapes, indicating that both AMUs belong to the same compound (i.e., N_2O). This finding applies to all of the catalysts studied in the temperature range of 373–873 K. Thus, no nitric oxide (NO) as an intermediate gas-phase product was observed on N_2O decomposition over Fe-ZSM-5 and Rh-ZSM-5 under transient conditions of the TAP reactor; the only products detected were O_2 and N_2.

The order of appearance and the shapes of N_2O, N_2, and O_2 transient responses in Fig. 7 were analyzed in more detail (Fig. 8). For Rh-ZSM-5, the times of maximum (t_{max}) of the N_2 transient response (0.119 s at 623 K and 0.057 s at 723 K) and the O_2 transient response (0.120 s at 623 K and 0.058 s at 723 K) were very similar, and both were significantly longer than that of the N_2O transient response (0.047 s at 623 K and 0.031 s at 723 K). In contrast to Rh-ZSM-5, the t_{max} of N_2O and N_2 over Fe-ZSM-5 were very similar but significantly shorter than that of the O_2 transient response. The t_{max} values of O_2, N_2, and N_2O transients over the catalysts at different temperatures are compared in Fig. 8. The t_{max} of N_2 and O_2 transients over Rh-ZSM-5 similarly decreased with increasing reaction temperature; however, for Fe-ZSM-5, the t_{max} of the O_2 transient response decreased with temperature more strongly than that of N_2. Moreover, the reaction temperature influenced the shape of the O_2 response in a different manner (Fig. 7). The most significant changes were observed for Fe-ZSM-5, in which the temperature increase from 723 to 823 K led to a six-fold narrowing of the oxygen transient response. For Rh-ZSM-5, the O_2 transients also narrowed with increasing temperature, but demonstrated a characteristic tailing (i.e., a slow decrease in concentration with time). The foregoing analysis of the t_{max} values provides qualitative information on the mechanistic differences of direct N_2O decomposition over Fe-ZSM-5 and Rh-ZSM-5. In contrast to Rh-ZSM-5,

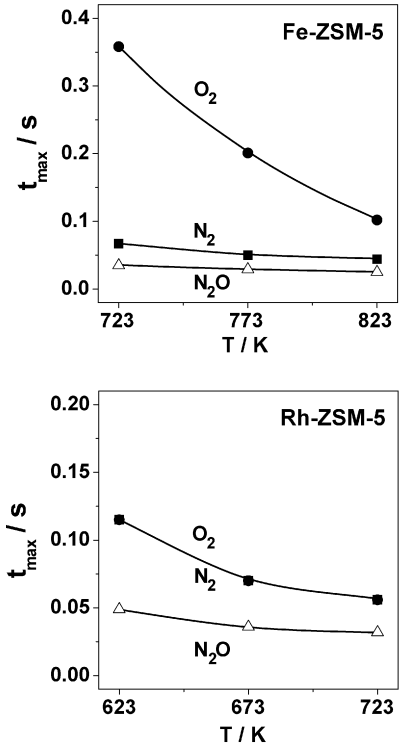

Fig. 8. Characteristic times of the transient responses of N_2O, N_2, and O_2 upon N_2O pulsing over Rh-ZSM-5 (10 mg), and Fe-ZSM-5 (25 mg) at different temperatures (N_2O:Ne = 1:1, pulse size ca. 10^{15}).

reaction pathways leading to O_2 formation over Fe-ZSM-5 were slower than those leading to N_2. Moreover, O_2 formation generally was much easier over Rh-ZSM-5 than over Fe-ZSM-5.

3.4. Microkinetic analysis

The transient responses of N_2O, N_2, and O_2 derived from the N_2O pulse experiments in the TAP reactor were simultaneously fitted to the microkinetic models listed in Table 1. Considering the structure of the active metal sites in the zeolite or the charge of oxygen species adsorbed on these sites is beyond the scope of our modeling approach. In all of the models evaluated, N_2O decomposition is initiated by deposition of active oxygen species over free active sites (*) either directly from gas-phase N_2O (models 1–5) or via decomposition of adsorbed N_2O (models 6–11). The models differ basically in terms of the reaction pathways leading to O_2. Models 1, 6, and 10 consider O_2 formation via direct recombination of two mono-atomic *-O species, as suggested in [23,25]. O_2 formation via decomposition of a surface bi-atomic oxygen precursor is incorporated in models 3, 7, and 9 [30,55,56]. Models 2 and 8 assume a direct reaction of gas-phase N_2O with *-O, leading to gas-phase O_2 [27]. This reaction pathway is modified in models 4, 5, and 9 assuming that bi-atomic or tri-atomic oxygen species are formed on interaction of gas-phase N_2O with mono-atomic *-O species of bi-atomic O-*-O species, respectively, as previously suggested in [35,36]. In model 11, desorption of surface *-O_2 species is a reversible process.

3.4.1. Fe-ZSM-5

Because the N_2O adsorption/desorption properties of Fe-ZSM-5 could not be unambiguously determined even at 373 K, adsorption of N_2O was not considered for this catalyst in our kinetic approach in the temperature range 723–773 K. Transient responses of N_2O, N_2, and O_2 obtained during N_2O decomposition over Fe-ZSM-5 were fitted to models 1–5. The reaction scheme in model 5 provided the best description of all transient responses in the temperature range investigated (Fig. 9). As reported previously [36], model 5 described well the N_2O decomposition over steam-activated Fe-silicalite and Fe-ZSM-5 having mostly isolated and oligonuclear iron species, respectively; therefore, the mechanistic scheme of N_2O decomposition derived over steam-activated Fe-silicalite and Fe-ZSM-5 [36] was extended for the ion-exchanged Fe-ZSM-5, which has larger iron oxide particles (see the TEM images in Fig. 3). Another important conclusion is that the reaction mechanism of N_2O decomposition is the same over Fe-ZSM-5 pretreated in a He flow at 873 K [36] and in an O_2 flow at 873 K (in the present work). Moreover, steam activation of Fe-ZSM-5 did not appear to influence the mechanism of N_2O decomposition. The only difference between the steam-activated and the ion-exchanged Fe-ZSM-5 is in the kinetic parameters of N_2O decomposition in Table 3. It should be mentioned that these kinetic parameters were extrapolated to 573 K using the Arrhenius equation, to properly compare the differences between Rh-ZSM-5 and Fe-ZSM-5 materials in their low-temperature de-N_2O activity. In

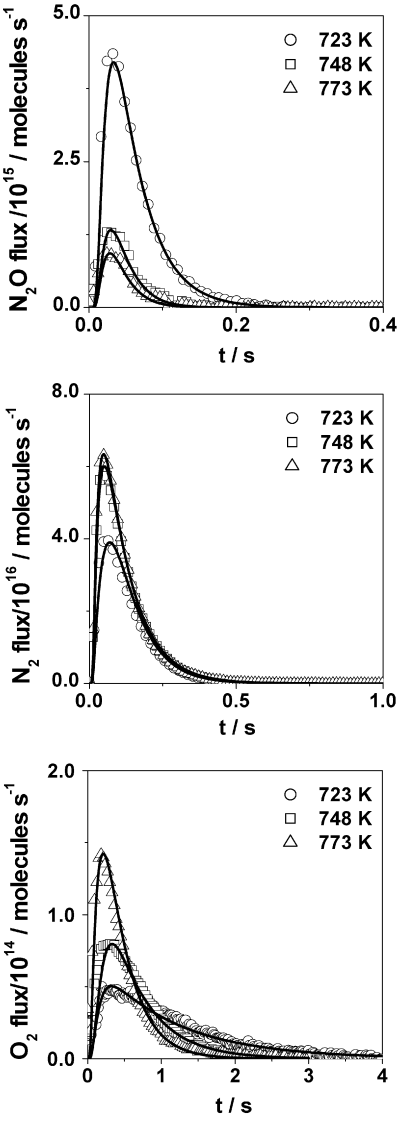

Fig. 9. Experimental (open symbols) and calculated (lines) transient responses of N_2O, N_2, and O_2 using different models for N_2O decomposition over Fe-ZSM-5 at different temperatures.

agreement with the order of steady-state activity in N_2O decomposition [15], the steam-activated Fe-ZSM-5 had higher reaction constants of N_2O decomposition compared with the ion-exchanged Fe-ZSM-5.

Summarizing, our microkinetic evaluation predicts that independent of the nature of iron species and activation procedure of Fe-ZSM-5, iron sites as well as those with deposited monoatomic oxygen species, are active for N_2O decomposition. Oxygen formation occurs via two steps. First, a bi-atomic oxygen precur-

Table 3
Best kinetic model and parameters of N_2O decomposition over ion-exchanged Fe-ZSM-5 and steam-activated Fe-ZSM-5 [36] derived from transient experiments in the TAP reactor

No.	Elementary reaction steps	Ion-exchanged Fe-ZSM-5		Steam-activated Fe-ZSM-5	
		$k_{573\,K}$ (s^{-1})	E_a (kJ mol^{-1})	$k_{573\,K}$ (s^{-1})	E_a (kJ mol^{-1})
1	$N_2O + * \rightarrow$ *-O + N_2	4.9×10^{-6}[a]	130	3.4×10^{-4}[a]	69
2	N_2O + *-O $\rightarrow$ O-*-O + N_2	1.5×10^{-5}[a]	112	2.7×10^{-5}[a]	98
3	O-*-O $\rightarrow$ *-O_2	7×10^{-2}	61	4.5×10^{-2}	142
4	*-$O_2 \rightarrow O_2 + *$	4.1×10^{3}	58	5.7×10^{-1}	50

[a] Reaction constant in $Pa^{-1}\,s^{-1}$.

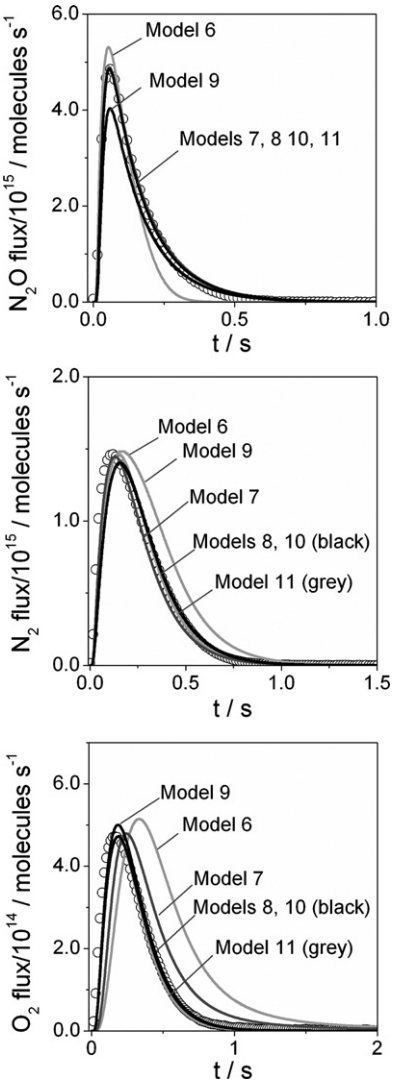

Fig. 10. Experimental (open symbols) and calculated (lines) transient responses of N_2O, N_2, and O_2 using different models for N_2O decomposition over Rh-ZSM-5 (at 573 K).

sor (O-*-O) is formed on N_2O decomposition over iron site with mono-atomic adsorbed oxygen species (Eq. 2 in model 5). Then this bi-atomic precursor is transformed into another bi-atomic oxygen species (*-O_2, Eq. 3 in model 5), which decomposes yielding gas-phase O_2 and a free site (Eq. 4 in model 5).

3.4.2. Rh-ZSM-5

It should be stressed that kinetic evaluation of N_2O decomposition over Rh-ZSM-5 was performed in the temperature range of 573–723 K. Because the kinetic evaluation over Fe-ZSM-5 was done at 723 K as well, we can conclude that the derived mechanistic differences in both catalytic systems are comparable. Fig. 10 shows the experimental transient responses of N_2O, N_2, and O_2 on pulsing N_2O over Rh-ZSM-5 at 573 K and the responses calculated applying models 6–11 with optimized kinetic parameters. According to the results discussed in Section 3.3, all of these reaction schemes start with reversible N_2O adsorption over free (*) active cites, followed by decomposition of adsorbed N_2O to gas-phase N_2 and surface oxygen species (*-O). Models 6 and 9 did not provide a good description of the experimental transient responses. The fitting of the N_2O and N_2 responses with models 7, 8, 10, and 11 was reasonable; however, the experimental O_2 response was poorly predicted by model 7. Models 8, 10, and 11 provided

Table 4
Best kinetic model and parameters of N_2O decomposition over Rh-ZSM-5 derived from transient experiments in the TAP reactor

No.	Elementary reaction steps	$k_{573\,K}$ (s^{-1})	E_a (kJ mol^{-1})
1	$N_2O + * \rightarrow$ *-N_2O	1.1×10^{-2}[a]	10
2	*-$N_2O \rightarrow N_2O + *$	93	81
3	*-$N_2O \rightarrow$ *-$O + N_2$	26	120
4	$N_2O +$ *-$O \rightarrow * + O_2 + N_2$	2.8×10^{-2}[a]	83
5	$O_2 + * \rightarrow$ *-O_2	2.4×10^{-12}[a]	10
6	*-$O_2 \rightarrow O_2 + *$	0.17	29
7	*-$O_2 + * \rightarrow$ 2*-O	3.7	250
8	2*-O $\rightarrow$ *-$O_2 + *$	454	168

[a] Reaction constant in $Pa^{-1}\,s^{-1}$.

the best overall description of the N_2O, N_2, and O_2 responses. The first three reaction steps in the latter three models are the same: N_2O adsorption and desorption, decomposition of adsorbed N_2O to gas-phase N_2 and *-O, and finally reaction of gas-phase N_2O with *-O to gas-phase O_2 and N_2. Model 10 includes one additional reaction step: recombination of two *-O to gas-phase O_2. According to model 11, O_2 formed via reaction of gas-phase N_2O with *-O readsorbed reversibly and dissociatively via a bi-atomic precursor.

Because the correct description of data obtained over a broad temperature range is an important criterion for model discrimination, simultaneous fitting of N_2O, N_2, and O_2 transient responses was performed in the temperature range of 573–723 K using models 8, 10, and 11. Model 11 properly predicted the experimental results, whereas models 8 and 10 did not. This indicates that N_2O decomposition over Rh-ZSM-5 is initiated by reversible N_2O adsorption over free Rh sites, followed by its decomposition into N_2 and active oxygen species (*-O). In agreement with the findings of Kunimori et al. [39,40], oxygen formation over Rh black and Rh/USY occurs through recombination of two active oxygen species (*-O). In addition to this reaction step, however, our microkinetic model predicts that gas-phase O_2 also can be formed via reaction of gas-phase N_2O with surface oxygen species (*-O) originating from N_2O. The disagreement between our findings and those of Kunimori's group can be explained as follows. Kunimori et al. [39,40] studied N_2O decomposition over $^{18}O_2$-pretreated Rh black and Rh/USY and analyzed the distribution of labeled oxygen (^{18}O) in the formed gas-phase oxygen. For such an experimental approach, the possibility that surface oxygen species formed during $^{18}O_2$ pretreatment and those formed from N_2O have different reactivity toward N_2O decomposition cannot be excluded. This statement is indirectly supported by the conclusion of Kunimori et al. [39,40] that desorption of oxygen from the O_2-pretreated catalysts occurred at much higher temperatures than oxygen formation in N_2O decomposition.

3.4.3. Validation of TAP-derived microkinetic schemes

As discussed above, the derived mechanisms of N_2O decomposition correctly predict the transient behavior of N_2O decomposition over zeolites loaded with different active metals (model 11 for Rh-ZSM-5 and model 5 for Fe-ZSM-5). The next criterion that a model should fulfill is the dependence of the rate of N_2O decomposition on the inlet partial pressures of N_2O and O_2. For this purpose, we calculated the rates of N_2O decomposition under steady-state conditions using kinetic parameters derived from the fitting of TAP responses. The optimized kinetic parameters of direct N_2O decomposition over Fe-ZSM-5 and Rh-ZSM-5 are compared in Tables 3 and 4, respectively.

The rates were calculated at temperatures of 573–873 K and N_2O partial pressures of 1–10^3 Pa. The calculated rates are presented in Fig. 11. The rate of N_2O decomposition over Fe-ZSM-5 and Rh-ZSM-5 increased linearly with an increase in N_2O partial pressure. A slight deviation from a linear dependence above ca. 500 Pa can be predicted for Fe-ZSM-5 above 773 K. Similar be-

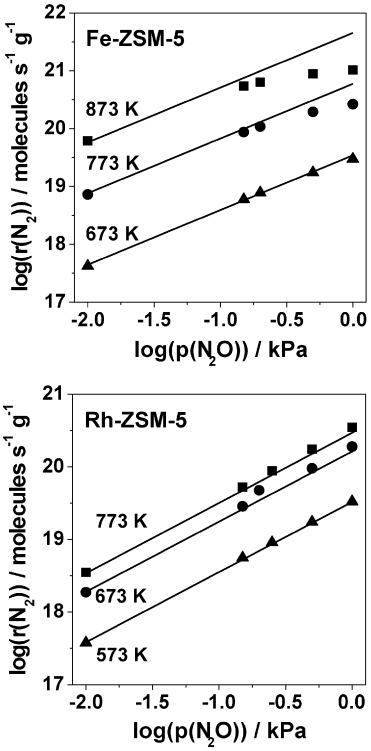

Fig. 11. Predicted reaction rates of N_2 formation upon N_2O decomposition over (a) Fe-ZSM-5 and (b) Rh-ZSM-5 at N_2O partial pressures and temperatures in the range of 10–10^3 Pa and 573–823 K, respectively. Calculations were performed with kinetic parameters from Tables 3 and 4. The lines show first-order dependence of the rate of N_2 formation on the inlet partial N_2O pressure.

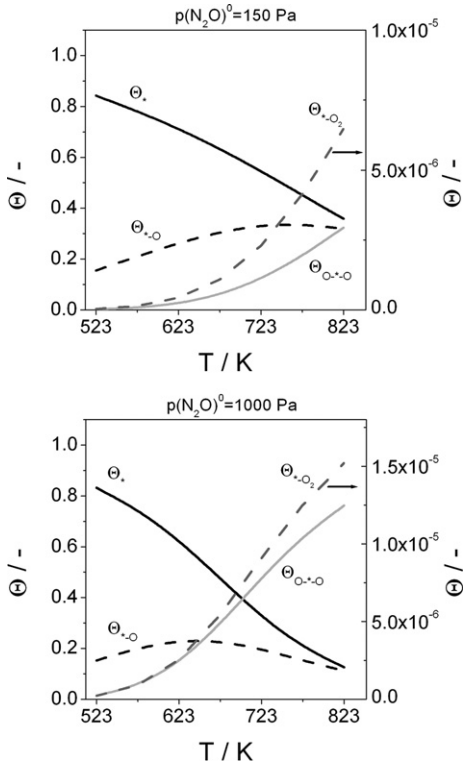

Fig. 12. Calculated steady-state coverage by surface species upon N_2O decomposition over Fe-ZSM-5 in the temperature range from 523 to 823 K for inlet N_2O partial pressures of 150 and 1000 Pa. Kinetic parameters from Table 3 were taken for the calculations.

havior was reported by Kapteijn et al. [25] for steady-state N_2O decomposition over ion-exchanged Fe-ZSM-5. They reported that even at low N_2O partial pressures (60–150 Pa), the reaction order of N_2O decomposition with respect to the N_2O partial pressure was <1 above 733 K.

According to the best microkinetic model of N_2O decomposition over Fe-ZSM-5 (Table 3), the formation of gas-phase O_2 via the desorption of molecular adsorbed oxygen (reaction step 4) is irreversible; therefore, gas-phase oxygen should not affect the rate of N_2O decomposition. This conclusion agrees with oft-reported steady-state performance of various Fe-ZSM-5 catalysts in N_2O decomposition [16,23,25,27–38]. However, our microkinetic evaluation made it possible to mechanistically explain the fact that O_2 formation limits N_2O decomposition even though oxygen does not inhibit N_2O decomposition. Our mechanistic scheme of N_2O decomposition predicts that the formation of gas-phase O_2 (reaction step 4) will be much faster than the surface rearrangement of one bi-atomic oxygen species to the molecular adsorbed oxygen (reaction step 3), which desorbs as O_2. Therefore, it is not the O_2 desorption, but rather the surface rearrangement, that limits the overall rate of O_2 formation and N_2O decomposition. This assumption is supported by the following discussion. Using kinetic parameters from Table 3, we calculated steady-state surface coverages for different temperatures and N_2O partial pressures. Fig. 12 shows the calculated coverages in the temperature range from 523 to 823 K for inlet N_2O partial pressures of 150 and 1000 Pa. The coverages by *, *-O, and O-*-O species were in the range 0.01–0.8, whereas the coverage by *-O_2 was very low, increasing from ca. 10^{-7} to 10^{-5} with an increase in temperature from 523 to 773 K. According to our microkinetic model, the rate of O_2 formation over Fe-ZSM-5 is proportional to this coverage. Such a low coverage can be easily understood by comparing the kinetic constants of *-O_2 formation and decomposition. The former is several magnitudes order lower than the latter. The complex mechanism of O_2 formation is a possible reason why O_2 formation limits N_2O decomposition without the inhibiting effect of O_2.

In contrast to Fe-ZSM-5, oxygen should inhibit N_2O decomposition over Rh-ZSM-5 (Table 4). To quantify the effect of oxygen over Rh-ZSM-5, we calculated the rates of N_2O decomposition at different N_2O (1–1000 Pa) and O_2 (1–10,000 Pa) partial pressures. No inhibiting effect of N_2O could be predicted. This can be explained by the fact that the rate constant of the interaction of O_2 with free Rh sites is ca. 10^{10} times lower than that for the N_2O reaction; therefore, oxygen should inhibit N_2O decomposition only at very low N_2O/O_2 ratios.

Summarizing the foregoing results, we can conclude that the transient performance of Fe-ZSM-5 and Rh-ZSM-5 in direct N_2O decomposition can be quantitatively described by two microkinetic models differing in terms of N_2O adsorption properties and the pathways for N_2 and O_2 formation. Both models predict first-order dependence of N_2O decomposition on the partial pressure of N_2O and no inhibiting effect of O_2 on N_2O decomposition under steady-state conditions. In the next section we discuss possible origins of the significant low-temperature activity of Rh-ZSM-5 compared with Fe-ZSM-5 on the basis of our microkinetic analysis.

3.5. Mechanistic origins of catalytic activity in N_2O decomposition

According to the TAP-derived microkinetic schemes, both free metal sites (*) and surface mono-atomic oxygen species (*-O) participate in N_2O decomposition over Fe-ZSM-5 and Rh-ZSM-5. For Fe-ZSM-5, gas-phase N_2O decomposes directly over a free iron site (reaction step 1 in Table 3), whereas for Rh-ZSM-5, adsorbed N_2O yields gas-phase N_2 (reaction step 3 in Table 4). The calculated activation energies of these steps over ion-exchanged Fe-ZSM-5 and Rh-ZSM-5 were 130 and 120 kJ mol^{-1}, respectively. These similar values indicate that the strength of nitrogen–oxygen bond in

the N_2O molecule mainly determines the energy costs required for N_2 formation. But the steam activation of Fe-ZSM-5 apparently results in a decrease in the activation energy of N_2O decomposition (69 kJ mol^{-1} in Table 3). This may be a reason for the beneficial effect of high-temperature steaming on the activity of Fe-ZSM-5, particularly below 673 K [15]. The overall rate constant of N_2O decomposition over free metal sites depends significantly not only on the metal in the zeolite, but also on the activation procedure of Fe-ZSM-5. As shown in Table 3, and Table 4, these rate constants were 4.9×10^{-6} Pa^{-1} s^{-1} over ion-exchanged Fe-ZSM-5, 3.4×10^{-4} Pa^{-1} s^{-1} over steam-activated Fe-ZSM-5, and 26 s^{-1} over Rh-ZSM-5 at 573 K. Because the respective activation energies do not differ significantly, such a great difference in the rate coefficients is determined by the pre-exponential factor (k^0), that is, collision frequencies of N_2O over Rh and Fe species. Based on the rate constants and activation energies given in Tables 3 and 4, we calculated the pre-exponential factors of N_2 formation using the Arrhenius equation. For N_2O decomposition over free metal sites, these factors were 3.4×10^6 Pa^{-1} s^{-1} for ion-exchanged Fe-ZSM-5, 6.7×10^2 Pa^{-1} s^{-1} for steam-activated Fe-ZSM-5, and 2.3×10^{12} s^{-1} for Rh-ZSM-5, indicating much higher collision frequencies of N_2O over Rh species than over Fe species. In contrast to N_2O decomposition over free active sites, k^0 of N_2 formation via interaction of gas-phase N_2O with surface oxygen species is not significantly influenced by the metal in the zeolite matrix. The calculated k^0 values for this reaction pathway were ca. 3×10^5 Pa^{-1} s^{-1} for ion-exchanged Fe-ZSM-5, 2.3×10^4 Pa^{-1} s^{-1} for steam-activated Fe-ZSM-5, and 1.5×10^6 Pa^{-1} s^{-1} for Rh-ZSM-5, with corresponding activation energies of 112, 89, and 83 kJ mol^{-1}. Thus, from a kinetic standpoint, we posit that the metal's N_2O-adsorptive property is an essential feature affecting the rate of N_2O decomposition. Kiwi-Minsker et al. [16,24] and Ates and Reitzmann [33] have noted that N_2O adsorption should be taken into consideration in describing N_2O decomposition over Fe-ZSM-5 catalysts; however, they did not attempt to correlate the catalysts' de-N_2O activity and N_2O-adsorptive properties.

Another key mechanistic dissimilarity between Rh-ZSM-5 and Fe-ZSM-5 relates to the pathway for O_2 formation, which is often discussed as the rate-limiting step of N_2O decomposition [16,23, 28–31]. There are two parallel reaction pathways of O_2 formation over Rh-ZSM-5: (i) Oxygen originates via recombination of two active oxygen species (*-O) and (ii) N_2O interacts with a surface mono-atomic oxygen species (*-O), yielding gas-phase O_2 and N_2. Our calculations predict that the former reaction pathway dominates above 623 K. At lower temperatures, at which Kunimori et al. [39,40] analyzed N_2O decomposition over Rh-USY, both reaction pathways of O_2 formation contribute equally to the overall O_2 formation. In contrast to Rh-ZSM-5, oxygen formation over Fe-ZSM-5 occurs via a complex sequence of three elementary reaction pathways: (i) N_2O reacts with an active oxygen species (*-O), yielding an adsorbed bi-atomic oxygen species (O-*-O); (ii) the formed bi-atomic oxygen species intermediate reorganizes into another bi-atomic one (*-O_2); and (iii) *-O_2 desorbs as O_2, generating free-iron sites. The overall oxygen production over Fe-ZSM-5 is limited by the rearrangement of one adsorbed bi-atomic oxygen species to another.

In summary, we have identified two possible mechanistic origins of the superior low-temperature activity of Rh-ZSM-5 over Fe-ZSM-5: (i) Rh presents stronger reversible N_2O adsorption, which significantly influences the rate constant of N_2O decomposition over free metal sites, yielding N_2 and active oxygen species (*-O); and (ii) oxygen formation occurs directly via reaction of gas-phase N_2O with *-O over Rh-ZSM-5. These are of fundamental importance because they provide insight into the reaction mechanism, and they can be applied to the design of novel catalytic materials (e.g., nonnoble metal-containing or alloys) for applications in which N_2O should be eliminated at low temperatures. In principle, the mechanistic "fingerprints" identified in this study demonstrate the category of the catalyst with respect to its operation temperature and can provide an alternative to traditional steady-state tests as a screening tool. We expect our findings to stimulate theoreticians to confirm our conclusions on a molecular level.

4. Conclusion

Transient studies of N_2O decomposition over Rh-ZSM-5 and Fe-ZSM-5 in the TAP reactor have established that the activity order of the catalysts is not influenced by the mode of reactor operation (steady-state ambient pressure vs transient vacuum); Rh-ZSM-5 showed remarkably higher activity for N_2O decomposition below 573 K than Fe-ZSM-5. Possible mechanistic origins of Rh-ZSM-5's greater catalytic activity were derived from a quantitative microkinetic analysis of N_2O decomposition, according to which transient responses of N_2O, N_2, and O_2 were fitted simultaneously to different microkinetic models. Through model discrimination, we concluded that classical reaction schemes are too simple to describe N_2O decomposition over both catalytic systems. Independent of the nature of active metal, both free metal sites and surface mono-atomic oxygen species formed from N_2O are active sites for N_2O decomposition. However, the microkinetic schemes of N_2O decomposition over Rh-ZSM-5 and Fe-ZSM-5 differ in the elementary reaction steps leading to N_2 and, more importantly, to O_2. N_2O reversibly adsorbs over Rh-ZSM-5 with subsequent decomposition of adsorbed N_2O species to gas-phase N_2 and surface mono-atomic oxygen species. Over Fe-ZSM-5 the later products are formed directly on the interaction of gas-phase N_2O with free iron sites. Oxygen formation over Fe-ZSM-5 occurs via a sequence of three elementary reactions. Surface transformation of a bi-atomic oxygen species to molecular adsorbed oxygen, which desorbs as O_2, limits overall O_2 formation and N_2O decomposition. The reaction mechanism over Fe-ZSM-5 is independent of the iron constitution induced by the preparation and activation routes (e.g., liquid-ion exchange vs steam activation), despite important differences in catalytic activity can be attained. In contrast to Fe-ZSM-5, O_2 is formed directly over Rh-ZSM-5 through the interaction of gas-phase N_2O with adsorbed mono-atomic oxygen species originating from the decomposition of adsorbed N_2O. Based on our findings, we can conclude that reversible N_2O adsorption and rapid oxygen formation appear to be essential features for low-temperature catalytic N_2O decomposition.

Acknowledgments

This work was partially supported by Deutsche Forschungsgemeinschaft (DFG) within the collaborative research center (Sonderforschungsbereich) 546 "Structure, dynamics and reactivity of transition metal oxide aggregates." Financial support from the Spanish MEC (project CTQ2006-01562/PPQ and Consolider-Ingenio 2010 grant CSD2006-00003) and the ICIQ Foundation is also acknowledged.

Appendix A. Quantification of transient responses

The relative sensitivities (A_i^r) of feed components and reaction products in mass spectrometric analysis were determined as the ratio of the areas under the response signals of each compound related to the area under the response signal of the inert gas (Ne). The respective areas were corrected according to the contribution of fragmentation pattern of the different compounds to the measured AMU signal. Mole fractions of gas-phase components were calculated according to Eq. (A.1). Calculation of conversion and yield was performed using Eqs. (A.2) and (A.3), respectively. In

these expressions, $A^r_{\mathrm{exp},i}$ is the relative sensitivity observed over each catalyst, $A^r_{\mathrm{cal},i}$ is the relative sensitivity determined separately for the same reactant mixture in the reactor filled with inert material, κ_{inert} is the mole fraction of inert gas in the reactant mixture, $\kappa^0_{\mathrm{educt}}$ is the molar fraction of reactant at the reactor inlet, and $\kappa^{\mathrm{out}}_{\mathrm{educt}}$ is the mole fraction of reactant at the reactor outlet,

$$\kappa_i = \frac{\kappa^0_{\mathrm{inert}} \cdot A^r_{\mathrm{exp},i}}{A^r_{\mathrm{cal},i}}, \tag{A.1}$$

$$X_i = \frac{A^r_{\mathrm{cal},i} - A^r_{\mathrm{exp},i}}{A^r_{\mathrm{cal},i}}, \tag{A.2}$$

$$Y_i = \frac{\nu_{\mathrm{educt}} \cdot \kappa_{\mathrm{product},i}}{\nu_{\mathrm{product},i} \cdot (\kappa^0_{\mathrm{N_2O}})}. \tag{A.3}$$

Appendix B. Kinetic evaluation of transient experiments

Mass balances for gas-phase and surface species were determined for each kinetic model in Table 1. As an example, Eqs. (B.1)–(B.5) represent these balances for model 1. In these equations, D_{eff} is the effective Knudsen diffusion coefficient, k_i is the rate coefficient, C_{total} is the total number of active sites, Θ_* is the fraction of free active sites, and $\Theta_{*\text{-O}}$ is the coverage by adsorbed monoatomic oxygen species. Similar expressions can be derived for models 2–11 in Table 1,

$$\frac{\partial C_{\mathrm{N_2O}}}{\partial t} = D_{\mathrm{eff}} \cdot \frac{\partial^2 C_{\mathrm{N_2O}}}{\partial x^2} - C_{\mathrm{total}} \cdot k_1 \cdot C_{\mathrm{N_2O}} \cdot (1 - \Theta_{*\text{-O}}) - C_{\mathrm{total}} \cdot k_2 \cdot C_{\mathrm{N_2O}} \cdot \Theta_{*\text{-O}}, \tag{B.1}$$

$$\frac{\partial C_{\mathrm{N_2}}}{\partial t} = D_{\mathrm{eff}} \cdot \frac{\partial^2 C_{\mathrm{N_2}}}{\partial x^2} + C_{\mathrm{total}} \cdot k_1 \cdot C_{\mathrm{N_2O}} \cdot (1 - \Theta_{*\text{-O}}) + C_{\mathrm{total}} \cdot k_2 \cdot C_{\mathrm{N_2O}} \cdot \Theta_{*\text{-O}}, \tag{B.2}$$

$$\frac{\partial C_{\mathrm{O_2}}}{\partial t} = D_{\mathrm{eff}} \cdot \frac{\partial^2 C_{\mathrm{O_2}}}{\partial x^2} + C_{\mathrm{total}} \cdot k_2 \cdot C_{\mathrm{N_2O}} \cdot \Theta_{*\text{-O}}, \tag{B.3}$$

$$\frac{\partial \Theta_{*\text{-O}}}{\partial t} = k_1 \cdot C_{\mathrm{N_2O}} \cdot (1 - \Theta_{*\text{-O}}) - k_2 \cdot C_{\mathrm{N_2O}} \cdot \Theta_{*\text{-O}}, \tag{B.4}$$

$$\sum \Theta_{\mathrm{i}} = \Theta_{*\text{-O}} + \Theta_* = 1. \tag{B.5}$$

The apparent diffusion coefficients of Ne ($D^{\mathrm{eff}}_{\mathrm{Ne}}$) were estimated at each temperature by fitting of the Ne transient responses assuming Knudsen diffusion model. The obtained coefficients were fixed and used for calculations of the respective values (D^{eff}_i) for N_2O, N_2, and O_2 according to Eq. (B.6), where M_{Ne} and M_i are the molecular weight of Ne and the i-component, respectively,

$$D^{\mathrm{eff}}_i = D^{\mathrm{eff}}_{\mathrm{Ne}} \sqrt{M_{\mathrm{Ne}}/M_i}. \tag{B.6}$$

References

[1] F. Kapteijn, J. Rodríguez-Mirasol, J.A. Moulijn, Appl. Catal. B 9 (1996) 25.
[2] Y. Li, J.N. Armor, Appl. Catal. B 1 (1992) L21.
[3] K. Doi, Y.Y. Wu, R. Takeda, A. Matsunami, N. Arai, T. Tagawa, S. Goto, Appl. Catal. B 35 (2001) 43.
[4] J. Pérez-Ramírez, F. Kapteijn, G. Mul, X. Xu, J.A. Moulijn, Catal. Today 76 (2002) 55.
[5] G. Centi, A. Galli, B. Montanari, S. Perathoner, A. Vaccari, Catal. Today 35 (1997) 113.
[6] G. Centi, L. Dall'Olio, S. Perathoner, Appl. Catal. A 194–195 (2000) 79.
[7] V. Centi, L. Dall'Olio, S. Perathoner, J. Catal. 194 (2000) 130.
[8] J. Oi, A. Obuchi, G.R. Bamwenda, A. Ogata, H. Yagita, S. Kushiyama, K. Mizuno, Appl. Catal. B 12 (1997) 277.
[9] S. Inamura, J.-I. Tadani, Y. Saito, Y. Okamoto, H. Jindai, C. Kaito, Appl. Catal. A 201 (2000) 121.
[10] J.N. Armor, T.A. Braimer, T.S. Farris, Y. Li, F.P. Petrocelli, E.L. Weist, S. Kannan, C.S. Swamy, Appl. Catal. B 7 (1996) 397.
[11] J. Oi, A. Obuchi, A. Ogata, G.R. Bamwenda, R. Tanaka, T. Hibino, S. Kushiyama, Appl. Catal. B 13 (1997) 197.
[12] J. Pérez-Ramírez, J. Overeijnder, F. Kapteijn, J.A. Moulijn, Appl. Catal. B 23 (1999) 59.
[13] J. Pérez-Ramírez, F. Kapteijn, J.A. Moulijn, Catal. Lett. 60 (1999) 133.
[14] M.C.E. Groves, R. Mauer, in: Proceedings of International Fertiliser Society, 2004, p. 1.
[15] J. Pérez-Ramírez, F. Kapteijn, J.C. Groen, A. Doménech, G. Mul, J.A. Moulijn, J. Catal. 214 (2003) 33.
[16] L. Kiwi-Minsker, D.A. Bulushev, A. Renken, J. Catal. 219 (2003) 273.
[17] G.D. Pirngruber, M. Luechinger, P.K. Roy, A. Cecchetto, P. Smirniotis, J. Catal. 224 (2004) 429.
[18] M. Kögel, R. Monnig, W. Schwieger, A. Tissler, T. Turek, J. Catal. 182 (1999) 470.
[19] G. Centi, F. Vazzana, Catal. Today 53 (1999) 683.
[20] P. Marturano, L. Drozdová, A. Kogelbauer, R. Prins, J. Catal. 192 (2000) 236.
[21] K.A. Dubkov, N.S. Ovanesyan, A.A. Shteinman, E.V. Starokon, G.I. Panov, J. Catal. 207 (2002) 341.
[22] J. Pérez-Ramírez, G. Mul, F. Kapteijn, J.A. Moulijn, A.R. Overweg, A. Doménech, A. Ribera, I.W.C.E. Arends, J. Catal. 207 (2002) 113.
[23] J. Pérez-Ramírez, F. Kapteijn, G. Mul, J.A. Moulijn, J. Catal. 208 (2002) 211.
[24] L. Kiwi-Minsker, D.A. Bulushev, A. Renken, Catal. Today 110 (2005) 191.
[25] F. Kapteijn, G. Marban, J. Rodriguez-Mirasol, J.A. Moulijn, J. Catal. 167 (1997) 256.
[26] B.R. Wood, J.A. Reimer, A.T. Bell, J. Catal. 209 (2002) 151.
[27] C.M. Fu, V.N. Korchak, W.K. Hall, J. Catal. 68 (1981) 166.
[28] G. Mul, J. Pérez-Ramírez, F. Kapteijn, J.A. Moulijn, Catal. Lett. 77 (2001) 7.
[29] G.D. Pirngruber, J. Catal. 219 (2003) 456.
[30] B.R. Wood, J.A. Reimer, A.T. Bell, M.T. Janicke, K.C. Ott, J. Catal. 224 (2004) 148.
[31] E.V. Kondratenko, J. Pérez-Ramírez, Appl. Catal. A 267 (2004) 181.
[32] D.A. Bulushev, L. Kiwi-Minsker, A. Renken, J. Catal. 222 (2004) 389.
[33] A. Ates, A. Reitzmann, J. Catal. 235 (2005) 164.
[34] A. Heyden, A.T. Bell, F.J. Keil, J. Catal. 233 (2005) 26.
[35] A. Heyden, F.J. Keil, B. Peters, A.T. Bell, J. Phys. Chem. B 109 (2005) 1857.
[36] E.V. Kondratenko, J. Pérez-Ramírez, J. Phys. Chem. B 110 (2006) 22586.
[37] E.V. Kondratenko, J. Pérez-Ramírez, Catal. Today 121 (2007) 197.
[38] N. Hansen, A. Heyden, A.T. Bell, F.J. Keil, J. Catal. 248 (2007) 213.
[39] S.-i. Tanaka, K. Yuzaki, S.-i. Ito, H. Uetsuka, S. Kameoka, K. Kunimori, Catal. Today 63 (2000) 413.
[40] S.-i. Tanaka, K. Yuzaki, S.-i. Ito, S. Kameoka, K. Kunimori, J. Catal. 200 (2001) 203.
[41] B.C. Lippens, J.H. de Boer, J. Catal. 4 (1965) 319.
[42] S. Brunauer, P.H. Emmett, E.J. Teller, J. Am. Chem. Soc. 60 (1938) 309.
[43] J.T. Gleaves, G.S. Yablonsky, P. Phanawadee, Y. Schuurman, Appl. Catal. A 160 (1997) 55.
[44] J. Pérez-Ramírez, E.V. Kondratenko, Catal. Today 121 (2007) 160.
[45] M. Rothaemel, M. Baerns, Ind. Eng. Chem. Res. 35 (1996) 1556.
[46] M. Soick, D. Wolf, M. Baerns, Chem. Eng. Sci. 55 (2000) 2875.
[47] R.F. Sinkovek, N.K. Madsen, ACM Transactions on Mathematical Software 1 (1975) 232.
[48] D. Wolf, R. Moros, Chem. Eng. Sci. 52 (1997) 1189.
[49] W.H. Press, B.P. Flannery, S.A. Teukolsky, W.T. Vetterling, Numerical Recipes in FORTRAN, Cambridge University Press, Cambridge, 1992, p. 402.
[50] O.P. Keipert, M. Baerns, Chem. Eng. Sci. 53 (1998) 3623.
[51] G.E.P. Box, N.R. Draper, Empirical Model-Building and Response Surfaces, Wiley & Sons, New York, 1987.
[52] D.M. Bates, D.G. Watts, Nonlinear Regression Analysis and Its Application, John Wiley & Sons, New York, 1988.
[53] J. Pérez-Ramírez, F. Kapteijn, G. Mul, J.A. Moulijn, Chem. Commun. (2001) 693.
[54] G. Grubert, M.J. Hudson, R.W. Joyner, M. Stockenhuber, J. Catal. 196 (2000) 126.
[55] A.L. Yakovlev, G.M. Zhidomirov, R.A. van Santen, Catal. Lett. 75 (2001) 45.
[56] J.A. Ryder, A.K. Chakraborty, A.T. Bell, J. Catal. 220 (2003) 84.